Evolution of pitch angle distributions of relativistic electrons during geomagnetic storms: Van Allen Probes Observations

Ashley D. Greeley[1], Shrikanth G. Kanekal[1], David G. Sibeck[1], Quintin Schiller[2], Daniel N. Baker[3]

[1]NASA Goddard Space Flight Center,Greenbelt, MD, USA
[2]Space Science Institute, Fort Atkinson, WI, USA
[3]Laboratory for Atmospheric and Space Physics, University of Colorado Boulder, Boulder, CO, USA

Key Points:

- The evolution of electron pitch angle distributions can be tracked well by a pitch angle index, 'n' in $J_0 sin^n \theta$
- Ultra relativistic electrons consistently have a higher n than relativistic electrons
- Isotropization rates can be linearly fit and statistically differ between CME- and CIR-driven storms

Corresponding author: Ashley Greeley, ashley.greeley@nasa.gov

Abstract

We present a study analyzing relativistic and ultra relativistic electron energization and the evolution of pitch angle distributions using data from the Van Allen Probes. We study the connection between energization and isotropization to determine if there is a coherence across storms and across energies. Pitch angle distributions are fit with a $J_0 sin^n\theta$ function, and the variable 'n' is characterized as the pitch angle index and tracked over time. Our results show that, consistently across all storms with ultra relativistic electron energization, electron distributions are most anisotropic within around a day of Dst_{min} and become more isotropic in the following week. Also, each consecutively higher energy channel is associated with higher anisotropy after storm main phase. Changes in the pitch angle index are reflected in each energy channel; when 1.8 MeV electron pitch angle distributions increase (or decrease) in pitch angle index, so do the other energy channels. We show that the peak anisotropies differ between CME- and CIR- driven storms and measure the relaxation rate as the anisotropy falls after the storm. The isotropization rate in pitch angle index for CME-driven storms is -0.15±0.02 day^{-1} at 1.8 MeV, -0.30±0.01 day^{-1} at 3.4 MeV, and -0.39±0.02 day^{-1} at 5.2 MeV. For CIR-driven storms, the isotropization rates are -0.10±0.01 day^{-1} for 1.8 MeV, -0.13±0.02 day^{-1} for 3.4 MeV, and -0.11±0.02 day^{-1} for 5.2 MeV. This study shows that there is a global coherence across energies and that storm type may play a role in the evolution of electron pitch angle distributions.

Plain Language Summary

Using Van Allen Probes data, we measure pitch angle distributions of relativistic and ultra relativistic electrons. Anisotropic pitch angle distributions are sharply peaked around 90 degrees. More evenly distributed pitch angles are isotropic. Our results show that, consistently across all storms with ultra relativistic electron enhancements, electrons are most anistropic within around a day of storm onset and slowly isotropize in the following week. In addition, each consecutively higher energy channel is also associated with higher anisotropy after the main phase of geomagnetic storms, a characteristic which holds through the storm and recovery. Changes in the pitch angle index are reflected in each energy channel; when 1.8 MeV electrons increase (or decrease) in pitch angle index, so do all the other energy channels. In a superposed epoch study, we show that the peak anisotropies differ between different storm drivers (namely, coronal mass ejections and corotating interaction regions) and measure the isotropization rate as the anisotropy falls after the storm. This study shows that there is a global coherence across energies and that storm type may play a role in the evolution of electron pitch angle distributions.

1 Introduction

In the recent past, several space missions, including the Van Allen Probes (Mauk et al., 2013; D. Sibeck et al., 2012) and Arase (Miyoshi et al., 2018) have provided detailed observations of the Earth's radiation belts. They have not only revealed new phenomena (Baker et al., 2013), but also advanced our understanding of dynamics of electron energization and loss in the radiation belts. Both radial diffusion and wave-particle interactions (Baker et al., 2014; G. D. Reeves et al., 2013) lead to energization and loss of electrons in the outer Van Allen belt.

The importance of wave-particle interactions in both energizing and pitch angle scattering electrons is now well established. Chorus wave driven in-situ energization and subsequent ULF wave driven radial diffusion result in energization to relativistic and ultra-relativistic electrons (O'Brien et al., 2003; Claudepierre et al., 2008; Mourenas et al., 2014). Recent observations have shown direct evidence of pitch angle scattering (Fennell et al., 2014; Kasahara et al., 2018) as well as provided a comprehensive survey of energization time scales and associated wave phenomena (Baker et al., 2014). Observations have also shown cross-scale coupling between the lowest and highest energy electron populations. Low energy electrons have a pitch angle anisotropy which leads to wave generation, which in turn acts upon a "seed" population of "intermediate" energies, accelerating them to relativistic energies (Jaynes et al., 2015). Theoretical studies and modeling provide a robust frame-work for understanding the physical processes for the role of various plasma waves affecting electron dynamics (Summers et al., 1998; Thorne et al., 2013, 2013).

Despite the observational and theoretical advances, there are aspects of physical processes that drive the energization and loss which are not completely understood; for example the connection between pitch angle scattering, i.e., flux isotropization and electron enhancement has not been explored in detail. Early studies (G. Reeves et al., 1998) suggested that electrons with large pitch angles $\sim 90°$ are energized first, followed by isotropization. However, subsequent studies seemed to suggest that energization and isotropization were nearly simultaneous (Kanekal, 2006; Kanekal et al., 2005, 2001). These early studies were limited by insufficient temporal resolution (Kanekal et al., 1999), limited L coverage (Kanekal et al., 2001), and the use of multiple spacecraft in different orbits.

In this study, we use Van Allen Probes measurements to examine the relationship between electron energization and pitch angle distributions (PADs) during electron enhancements. We also analyze events driven by coronal mass ejections (CMEs) and corotating interaction regions (CIRs) separately. We perform superposed epoch analysis on the PAD evolution of relativistic and ultra-relativistic electron enhancements for 20 CME- and 24 CIR-driven events. The near-equatorial orbit of Van Allen Probes allows for large pitch angle coverage and the Relativistic Electron Proton telescope (REPT) measures electrons over a wide energy range with excellent pitch angle coverage (see Section 2).

PADs appear within the radiation belts in several distinctive shapes. These shapes are created by different mechanisms, such as wave-particle interactions or radial diffusion. Three common types of PADs are pancake, butterfly, and flat top (Chen et al., 2014). "Pancake" PADs peak at 90° and are thought to be caused by inward radial diffusion (Zhao et al., 2018) and/or wave-particle interactions (Ni et al., 2015). They are most prominent on the dayside (Gannon et al., 2007; West Jr. et al., 1973). The sharper the peak at 90°, the more anisotropic the PADs are. "Butterfly" distributions exhibit peak fluxes at $45° - 60°$ pitch angles and lower fluxes near-90° pitch angles, and could be caused by drift shell splitting (Stone, 1963) with or without magnetopause shadowing (Selesnick & Blake, 2002; D. G. Sibeck et al., 1987) in the outer belt. "Flat top" distributions have low fluxes at 0° and 180° and are flat over a range of pitch angles around 90°. These are considered isotropic. They could be a result of a transition between pancake and butterfly distributions, or could result from wave-particle interactions (Horne et al., 2003). Other types of pitch angle distributions can exist, but are less common (Zhao et al., 2018; Baker et al., 1978; D. G. Sibeck et al., 1987). Understanding the evolution of pitch angle distributions of different energetic populations, and the drivers that affect them, are essential to understand radiation belt physics.

Section 2 gives details regarding the instrument and spacecraft used in this study. The methods used to track pitch angle distributions over time are in Section 3. Results from single storm analysis and a statistical study are shown in Section 4. Section 5 contains a discussion on the results presented and potential drivers for the observations, and we conclude with a summary in Section 6.

2 Spacecraft and Data

This study uses data from NASA's Van Allen Probes mission (Mauk et al., 2013), consisting of two satellites launched in 2012 into a highly elliptical orbit ($\sim$500 to 30,000 km). Both identically instrumented spacecraft have sunward-pointing spin axes and spin

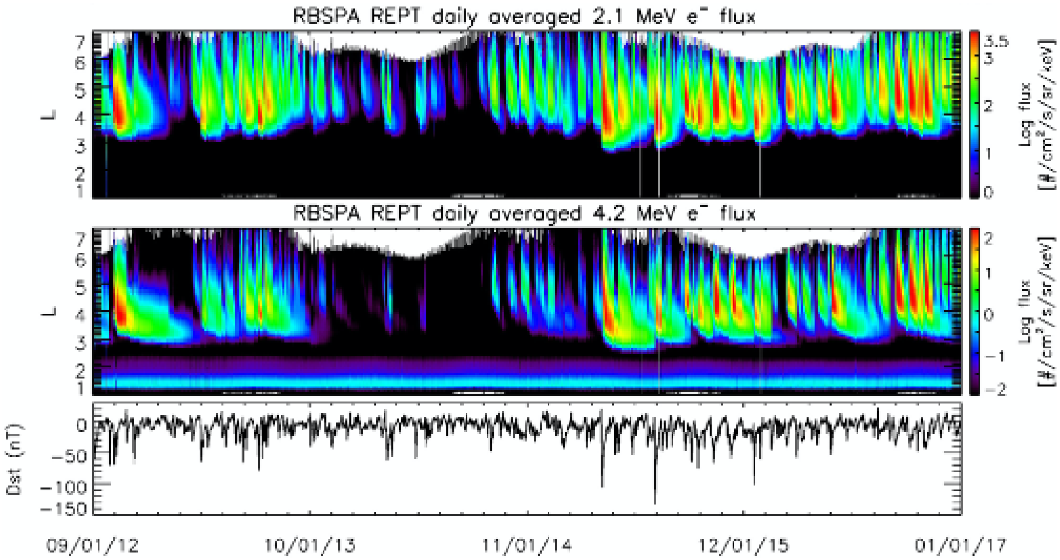

Figure 1. Lsort plots from RBSPA REPT channels from 2012-2017. The top panel is 2.1 MeV electrons and the middle panel represents 4.2 MeV electrons. The bottom panel shows Dst index. This figure is adapted from Zhao et al. (2018)

at ~6 rotations per minute (RPM) in the near-equatorial region at 10° inclination, allowing for broad sampling of pitch angles. They each carry five instrument suites to measure electrons, ions, plasma waves, and magnetic and electric fields. By using two spacecraft, the spatial and temporal extent of various phenomena can be measured. One laps the other every several months, allowing for a wide range of spatial measurements. The prime mission lifetime for Van Allen Probes was two years, but both spacecraft collected data for over seven years. The Van Allen Probes mission was launched near the peak of solar cycle 24, during which coronal mass ejections (CMEs) are more frequent, and covered the declining phase (mid-2014 through end of mission), when CIR/HSS are the dominant solar drivers.

The REPT instrument onboard the Van Allen Probes is a particle telescope comprising a stack of silicon solid-state detectors (SSDs) enclosed in aluminum-tungsten shielding. REPT measures charged electrons and protons with a geometry factor of 0.2 cm^2sr (Baker et al., 2012). It measures electrons ~2-20 MeV in 8 differential energy channels with an energy resolution ΔE/E of 30%. We can therefore observe PAD changes from the relativistic to ultra relativistic energy regime using a single instrument. Van Allen Probes passes through the inner and outer belts during its orbit, and maps both these regions well over long periods of time.

Figure 1, adapted from Figure 2 of Zhao et al. (2018), shows REPT long-term Lsort plots from the 2.1 and 4.2 MeV electron energy channels, spanning 2012-2017. The figure shows color coded fluxes (top two panels) as indicated by the color bar to the right, as a function of time and L-shell. The bottom panel shows the Dst index. The L-shell is the McIlwain L parameter (McIlwain, 1961) and calculated using OP77Q (Olson & Pfitzer, 1977) for the external field and the IGRF (Finlay et al., 2010) internal field. L is a parameter that is defined using I and B_m, and remains constant along a magnetic field line (J. G. Roederer, 1967). Enhancements occur more frequently in the 2.1 MeV than the 4.2 energy channel .

3 Determining Pitch Angle Index

In this paper, we describe the characterization of pitch angle distributions of relativistic and ultra relativistic electrons in the REPT instrument and track this distribution over time. We will use this data to determine if there is a coherence in PAD changes across energies, if there is a pattern across storms, and if storm driver affects the pitch angle distribution of the electrons. To do so, we must first select time periods of enhanced relativistic and ultra relativistic electrons.

During 2012-2018, Zhao, Baker, Li, Jaynes, and Kanekal (2019) found that the only time that REPT observes electron enhancements in the >5.2 MeV energy channels was during geomagnetic storms, and, furthermore, that electrons of all energies observed by REPT were more likely to be enhanced after a storm, as compared to other time periods. Since REPT energy channels start at 1.8 MeV, the instrument exclusively measures relativistic and ultra relativistic electrons. Therefore, in order to study pitch angle distributions of electron populations up to ultra relativistic energies, we look for electron enhancements after geomagnetic storms. Around half of geomagnetic storms result in relativistic electron enhancements (G. D. Reeves et al., 2003).

In order to find storms with electron enhancements, we first selected days where the Dst index dropped below -40 nT and evaluated these time periods for ultrarelativistic enhancements. Following a method by Turner et al. (2015), we compared the maximum flux in each energy channel between 12 and 84 hours after the Dst_{min} to the maximum flux between 12 and 84 hours before the Dst_{min}. Electrons in a given energy channel are considered to be enhanced if the poststorm maximum flux is at least twice the prestorm maximum flux. There may only be flux enhancements in some energy channels, and indeed, we find that lower electron energy channels are more likely to be enhanced following a geomagnetic disturbance, in agreement with Zhao, Baker, Li, Jaynes, and Kanekal (2019). We selected storms that result in an electron enhancement in at least the REPT 1.8, 2.1, 2.6, and 3.4 MeV electron channels.

Next, we determined the likely storm driver, using OMNI data (available on CDAweb at https://cdaweb.sci.gsfc.nasa.gov) to plot storm characteristics, such as solar wind velocity, proton temperature in the solar wind, AE index, IMF B_z, and SYM-H. CME-driven storms tend to be have abrupt changes in AE, B_z, solar wind flow speed, and an increase in proton temperature shortly after storm commencement (Neugebauer & Goldstein, 2013). A CIR-driven storm tends to exhibit slower variations - solar wind velocity slowly increases, proton temperature in the solar wind may reach its max before storm commencement, and Dst (or SYM-H) index may be less intense and vary more during recovery (Jian, 1993). In addition, in a CIR-driven storm, B_z may fluctuate more, whereas in a CME-driven storm there is more often one a sudden drop. Not every storm will have each of these indicators, but together, they may point to the likely source of a geomagnetic storm. We corroborated our results from published storm lists as much as possible (Richardson & Cane, 2019; Shen et al., 2017; Bingham et al., 2018), and found them to be consistent with our categorization.

Pitch angle distributions within the radiation belts change as a function of L (Gannon et al., 2007), so choosing the L location in which to track pitch angle distributions is important. We want to track the pitch angle distribution of the enhanced electrons, therefore we select an L band centered around maximum electron intensity in the outer belt. This approach is the same as the one used by Blake et al. (2001). As they remark, "the electrons themselves are field line tracers". This technique reduces the dependence upon field model calculated quantities such as the L-shell . The L band extent must be optimized. On one hand, the L range cannot be too narrow, because the enhanced electrons drift inwards over the course of several days, and an overly narrow L range would lose important information regarding the enhanced population. On the other hand, attempting to fit the average pitch angle distribution over a very large L bin smooths out interesting features. We selected a bin size of 0.8 in L centered around the average max flux during the 5 days after Dst minimum to balance out these concerns. Neither shifting nor changing the size of the bin by several tenths in L changed the results of the analysis, which is likely due to the peak of electron flux dominating the average. In this way, as long as the maximum flux is within the L range, we are able to track the enhancement PAD well.

We obtained the average unidirectional differential electron flux (FEDU) for each energy channel, within the L range of interest, and in 10° pitch angle bins. Then, we interpolated over pitch angle and fit the distribution with the functional form $J_0 sin^n\theta$ between 50 and 130 degrees using a least square minimization (Moré, 1978). Here, 'n' is defined as the pitch angle index, as it will be referred to from this point on. We use a normalized root mean square error (RMSE) to determine goodness of fit of the functional form (Zhao et al., 2018; Ni et al., 2015; Carbary et al., 2011). The normalized RMSE is calculated as

$$RMSE = \frac{\sqrt{\sum_{k=0}^{K} (y_k - yfit_k)^2}}{\sqrt{K}(y_{max} - y_{min})} \tag{1}$$

where y_k is the flux at a given pitch angle. $yfit_k$ is the fitted flux at the same pitch angle, M is the total number of data points, and y_{max} and y_{min} are the flux maximum and minimum, respectively. The normalized RMSEs from all fitted PADs are nearly Gaussian on a log scale, with a mean at 0.01 and two standard deviations at 0.04 (to the right of the mean). All fits with an RMSE > 0.04 are excluded.

Butterfly pitch angle distributions are not well fit with a $sin^n\theta$ function, and are excluded from the study. Following the method outlined in Zhao et al. (2014), the average flux is calculated over a range of pitch angles. The average flux over a specific range is called an 'edge value', and is calculated as:

$$edge_{values} = f_{avg}(90^\circ - \alpha : 90^\circ + \alpha) \tag{2}$$

where $f_{avg}(a : b)$ is the average flux from pitch angle a to b. This edge value calculation is repeated for values of α from 5° to 45°. The maximum value of these 'edge values', multiplied by 0.95, is compared to the mean flux of $85^\circ - 95^\circ$ ('middle values'). If the middle values are lower than the edge values, the PAD is flagged as a butterfly distribution. Butterfly PADs most commonly result from drift shell splitting, which is more pronounced at high L shells (D. G. Sibeck et al., 1987). The average L range in this study is 3.9-4.7, so butterfly PADs are not a significant portion of the distribution types, particularly at the lower energy channels. In the discussion section, we discuss the butterfly occurrences found during storms with enhancements.

Figure 2 shows a few examples of REPT pitch angle distributions. The panel on the left shows 7 PADs that are well fit to the $sin^n\theta$ function. The color of each distribution is associated with its pitch angle index, shown to the left. The pitch angle index gives a numerical value to the anisotropy of the PAD. The pitch angle index does not take flux into account. The panel on the right shows 3 examples of butterfly distributions selected by our algorithm. These are excluded from the analysis. In both plots, the full PAD is shown in a light color, with the fit range in a more saturated color.

Pitch angle distributions that can be fit well with $J_0 sin^n\theta$ were compiled into a database. For each geomagnetic storm, there was a time series of pitch angle indices for each electron energy channel containing an enhancement. Within each selected storm, we study PADs of electrons covering a range of energies to determine if there is a coupling from relativistic (~1 MeV) to ultra relativistic (>3 MeV) energies by comparing the pitch angle index for energy channels over time. In addition, we compare PADs between storms

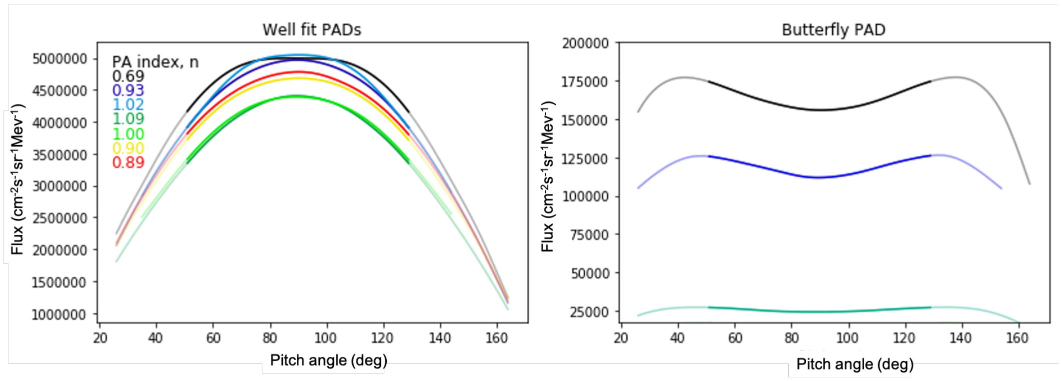

Figure 2. Example pitch angle distributions from REPT data in the 1.8 MeV electron bin. Plot on the left shows pitch angle distributions that are well fit to a $sin^n\theta$ function. The color of each pitch angle distribution is associated with a pitch angle index, 'n', from the fit to the data. The pitch angle index is shown to the left. The right plot shows a few examples of pitch angle distributions that the algorithm determined to be a butterfly pitch angle distribution. For each plot, the more saturated lines show where the data was fit.

to determine if there are similarities across storms, as well as storms grouped by solar drivers, i.e., CMEs and CIRs.

4 Results

4.1 Individual Storm Analysis

Firstly, we track the pitch angle index over time in each enhanced energy channel during individual storms. By analyzing a single storm at a time, it is possible to determine if there are any patterns across energy channels.

Figure 3 shows combined results from REPT probe A and B from a storm on June 29, 2015. The first three panels show electron flux as a function of L and time, color coded as shown in the color bars to the right of each panel. From top to bottom, the energy channels are 1.8, 3.4, and 7.7 MeV. The black dots indicate the location of maximum flux in L over each orbital pass. The L range analyzed in this storm was 3.4-4.2 in L. Panel (d) shows pitch angle index, 'n', as a function of time for electron energies ranging from 1.8 to 6.3 MeV. Energy channels are shown in different colors, from cool (purple, at 1.8 MeV) to warm (red, at 6.3 MeV). There were no pitch angle indices from the 7.7 MeV energy channel, as the analyzed unidirectional fluxes were not large enough to fit well to the $J_0 sin^n\theta$ distribution even if the fluxes were large enough to register as an enhancement. The error from the fit parameter (one standard deviation) are shown as pitch angle index errors. The bottom panel (e) shows Dst (nT) for the duration of the storm. Vertical lines show the time of minimum Dst.

The 1.8 MeV energy channel has a pitch angle index for every time the spacecraft travels through the outer belt. At higher energies, there are some gaps in the data. The gaps in pitch angle index for various energies are due to either low flux levels, high normalized RMSE value of the pitch angle distribution fit, or due to a measured butterfly distribution. The MLT of the data points are shown as a second x axis, and this particular plot is only for inbound passes of Van Allen Probes. The pitch angle distributions of the outer belt can vary over MLT, so we divided storms into inbound and outbound

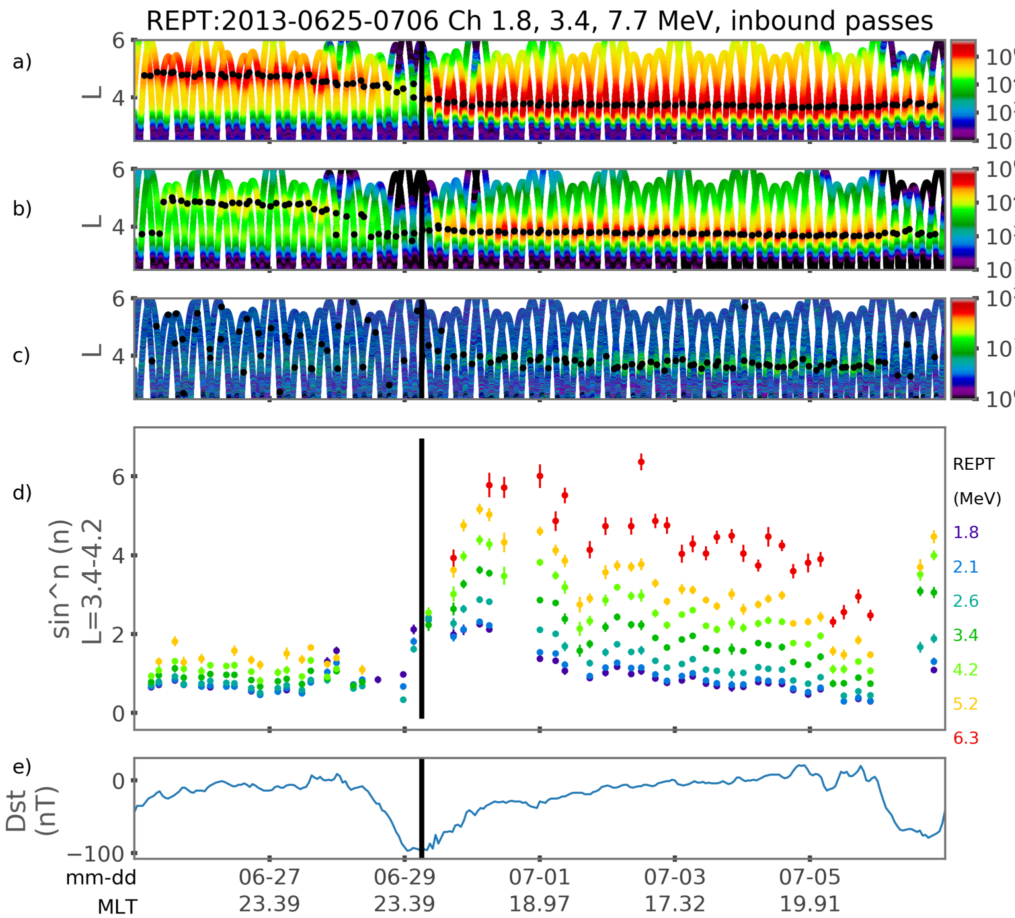

Figure 3. Fluxes of 1.8, 3.4, and 6.3 MeV electrons as a function of L (top three panels), color coded by flux, shown in the right for a storm on June 29, 2013. Black dots indicate the location in L of the flux maximum at each pass of the spacecraft through the outer belt. The fourth panel (d) shows pitch angle index (n) values for inbound passes of A and B. The bottom panel (e) shows the Dst index. Vertical black line indicates time of Dst_{min}, and MLT is shown as a second x-axis.

passes to be able to compare populations more directly within storms. These pitch angle indices are from the afternoon sector.

When the storm compressed the magnetosphere and the seed population energized, the resulting enhanced electrons are very anisotropic. The higher the energy channel, the more anisotropic the pitch angle distributions are. The pitch angle indices are most peaked within about one day of Dst_{min} and decrease until July 6, when there is another large drop in Dst. The highest energy electrons show up (at measurable values) within a few days of Dst_{min}. In this storm, the prestorm electron population is likely lost due to magnetopause shadowing (Turner et al., 2013).

Figure 4 shows the pitch angle index evolution for another storm, this one in March, 2019. The panels and markers are the same as in Figure 3. In this storm, the enhancement can only be measured up to the 5.2 MeV energy channel, and there appears to be

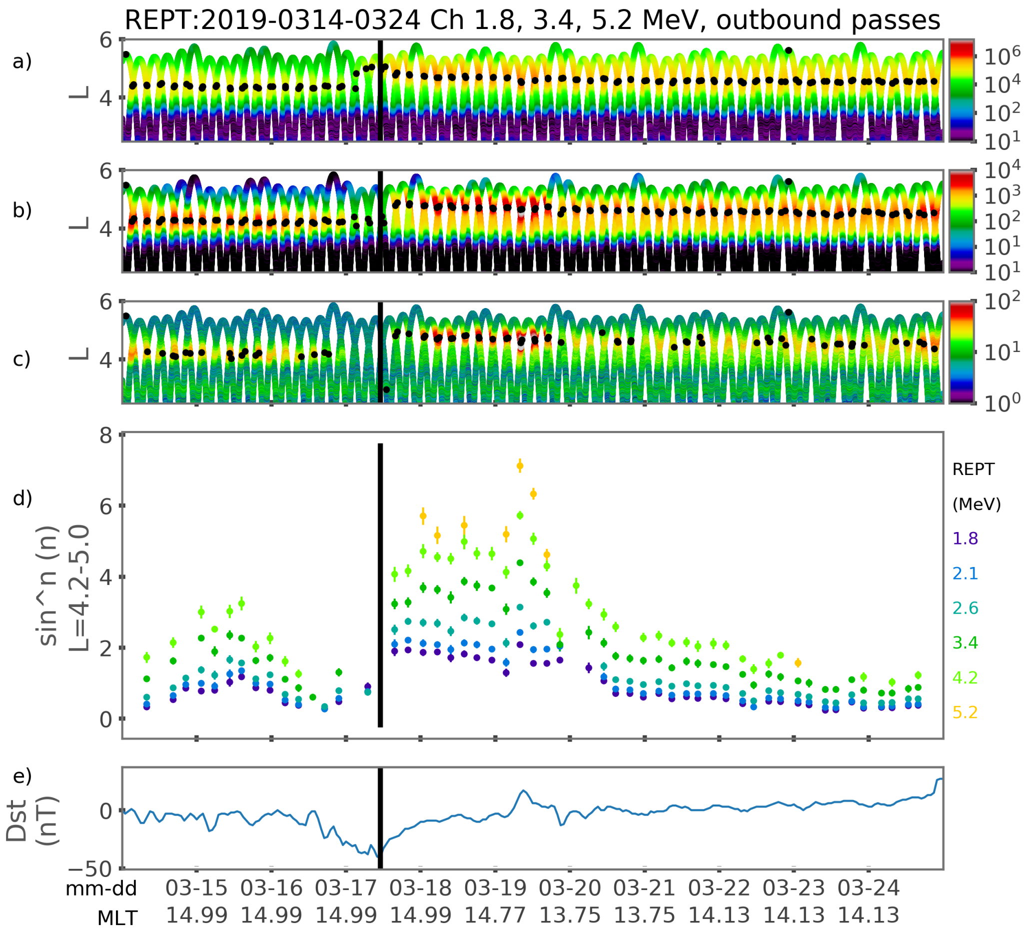

Figure 4. Fluxes of 1.8, 3.4, and 4.2 MeV electrons as a function of L (top three panels), color coded by flux, shown in the right for a storm on March 17, 2019. Black dots indicate the location in L of the flux maximum at each pass of the spacecraft through the outer belt. The fourth panel (d) shows pitch angle index (n) values for inbound passes of A and B. The bottom panel (e) shows the Dst index. Vertical black line indicates time of Dst_{min}, and MLT is shown as a second x-axis.

a second peak in the pitch angle index around 2 days after Dst_{min}. The higher energy electron channels are also associated with consistently higher anisotropies, and the patterns across energies are the same as for the previous storm.

It is well known that adiabatic effects may cause some of the pre storm electrons to appear to drop out, returning during the recovery phase of the storm (Li et al., 1997; Kim & Chan, 1997). Apparent dropouts, observed by sensors that measure differential intensities, could be adiabatic, i.e., due to geomagnetic field reconfiguration, which causes electron energies to change as the particles conserve their first adiabatic invariant. On the other hand, Turner et al. (2013) found that at $L > 4$, most losses are nonadiabatic and due to precipitation or magnetopause shadowing. In reality, the net flux is most likely a combination of adiabatic re-arrangement as well 'actual' loss. More recently, Hudson et al. (2014, 2015) analyzed flux dropout events observed by REPT. They used detailed MHD simulations to demonstrate that both magnetopause shadowing, as well as radial transport due to enhanced ULF wave power were needed to explain electron loss and changes to their PADs.

In Figure 4, the location in L of the pre and poststorm maximum electron populations differ by $\sim$0.4 R_E, which is expected from the conservation of adiabatic invariants. Kim and Chan (1997) calculate the expected energy changes due to adiabatic effects if the magnetic field at the before and after radial positions is known, as given below:

$$E_2 = -mc^2 + \sqrt{(mc^2)^2 + \frac{B_2(L_2)}{B_1(L_1)}(E_1^2 + 2mc^2E_1)} \tag{3}$$

where E_1 is the electron energy before the adiabatic rearrangement, E_2 is the energy after the adiabatic drift outwards, m is the mass of an electron, $B_1(L_1)$ is the magnetic field measured at the original position in L, and $B_2(L_2)$ is the magnetic field measured at the location in L after adiabatic rearrangement.

It is well known that the prestorm and poststorm electron fluxes are unrelated (G. D. Reeves et al., 2003). As they demonstrated, storms of similar strength resulted in enhancement, loss, or no change of pre- and post-storm fluxes. This implies that mere adiabatic rearrangement due to field configuration changes alone cannot explain poststorm fluxes. We show this explicitly below by starting with the assumption that the prestorm and poststorm electrons are of the same populations but that the drift shell has expanded, and assume that the electrons across relativistic and ultrarelativistic energies are in roughly the same location in L. The equation is for equatorially bouncing electrons, but serves as an estimate. On 3/16/19 (prestorm), the maximum 1.8 MeV electron flux is at L=4.63, and the magnetic field is 321 nT, calculated using the OP77Q model for the external and IGRF for the internal field in the REPT data files. On 3/18/19 (poststorm), the 1.8 MeV electron maximum is 5.05 in L and the calculated magnetic field is 236 nT. Using these numbers, we calculate the poststorm energies for several REPT channels. Electrons of energy 1.8 MeV before the storm onset would have 1.5 MeV in the poststorm population. Electrons of 3.4 MeV (as measured prestorm) would decrease in energy to 2.9 MeV. Electrons with energy 5.2 MeV would decrease to 4.4 MeV once the drift shell expands. However, as mentioned previously, REPT's higher energy channels are relatively empty before the geomagnetic storm (see Figure 4). While adiabatic changes could account for the main dropout during the Dst drop, the poststorm enhanced electron population is largely newly accelerated.

We emphasize that our focus is on the evolution of PADs of energized electrons during the recovery phase. By limiting our observations to a region (see discussion of L band above etc) around the position of the observed maximum of electron fluxes (Blake et al., 2001), as well as using observations of electrons over a wide energy range, we ensure that adiabatic effects have a minimal impact on our analysis (see discussion section for further details).

These plots show just 2 of the 43 storms analyzed for this study, but the qualitative characteristic of all of the storms are similar. In each of the storms analyzed, the characteristics of electron PADs during enhancement or energization evolve in a similar manner. When the pitch angle indices increased, they did so at every observed energy. A decrease in pitch angle index was similarly reflected across energy channels. This occurred for every time step within every storm. There is a clear coherence between relativistic and ultra relativistic enhancements. The changes that occur in tandem do so within the resolution of one orbital pass of Van Allen Probes, viz., ≈ 5 hours. In addition, the pitch angle index consistently increases with energy, i.e., the higher energy channels (6.3 MeV) are always associated with a higher pitch angle index than lower energy channels (1.8 MeV).

4.2 Superposed Epoch Study

Next, we investigate the average evolution of pitch angle distributions associated with electron energization. We will show that the pitch angle distributions of energized electrons change in the same manner over time for different storms. We conducted superposed epoch studies comparing evolution of electron PADs during CME-driven storms and CIR-driven storms. We found that there was an clear distinction between the pitch angle distribution evolution for different storm drivers.

We analyzed 20 CME- and 23 CIR-driven Van Allen Probes era storms with ultra relativistic enhancements. For each energy channel, the pitch angle indices were averaged in bin sizes of half a day, weighted by the error on their fit. The superposed epoch error was calculated as the relative error summed in quadrature. Bins with fewer than 1/5 of the total storms are not shown.

Figure 5 shows the resulting superposed epoch plot for CME-driven storms only, with electron energies ranging from 1.8-6.3 MeV. Figure 6 shows the superposed epoch plot for CIR-driven storms. Both Figure 5 and Figure 6 show superposed epoch curves for each energy in different colors (as indicated in the plot). For each energy, the thin darkest line is the weighted average pitch angle index (n), with 1 sigma and 2 sigma errors shown as shaded regions around the mean.

The pitch angle indices for CME-driven storms peak higher than CIR-driven storms. At 1.8 MeV, pitch angle indices (n) are 1.9 ± 0.1 and 2.1 ± 0.1 for CIR and CME-driven storms, respectively, and, similarly, 4.7 ± 0.2 and 5.6 ± 0.2 for 6.3 MeV electrons. CME-driven storms overall have a greater pitch angle distribution anisotropy in the day after Dst_{min} at relativistic and ultra relativistic energies.

We analyzed the isotropization rate from peak anistropy until 7 days after Dst_{min}. This was done for the superposed epoch of each energy channel and storm driver to determine how the average rate is different in each of these situations. The isotropization rate is well fit to a linear function.

Figure 7 compares the electron pitch angle indices for the 1.8, 3.4, and 5.2 MeV energy channels in CME- and CIR-driven storms and shows a linear fit to the isotropization rate of each energy. The figure shows superposed epoch curves corresponding to each energy in dark(light) colors for CME(CIR)-driven storms. The electron energy channels and solar driver types are indicated in the legend on the plot. The isotropization of of the pitch angle distributions is quantified by fitting the slope of the pitch angle distribution evolution for each of the electron energy bins for CME- and CIR-driven storms. The slopes and standard error on the slope is shown in the legend. The relaxation rate for CME-driven storms is -0.15 ± 0.02 day^{-1} at 1.8 MeV, -0.30 ± 0.01 day^{-1} at 3.4 MeV,

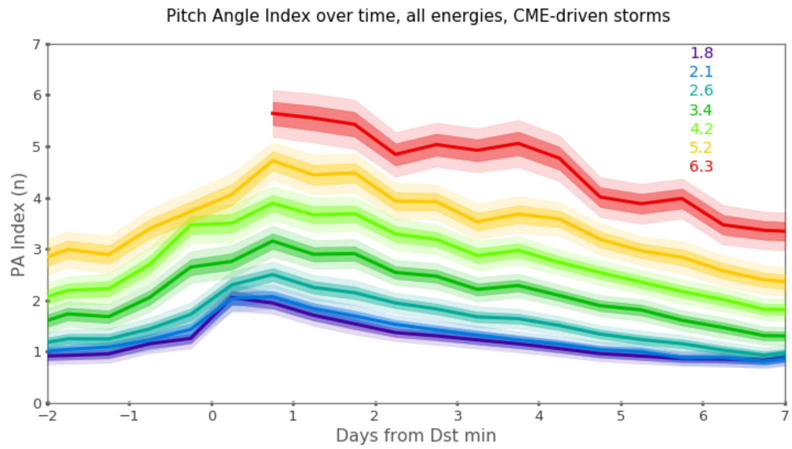

Figure 5. Superposed epoch study of PAD evolution for 20 CME-driven storms for energies 1.8-6.3 MeV. Color lines show weighted average PA index evolution, with lighter 1 sigma and 2 sigma error around the mean.

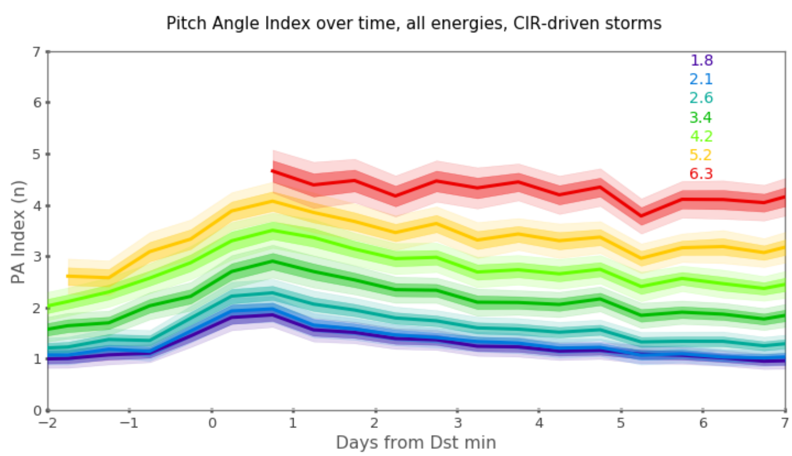

Figure 6. Superposed epoch study of PAD evolution for 23 CIR-driven storms for energies 1.8-6.3 MeV. Color lines show weighted average PA index evolution, with lighter 1 sigma and 2 sigma error around the mean.

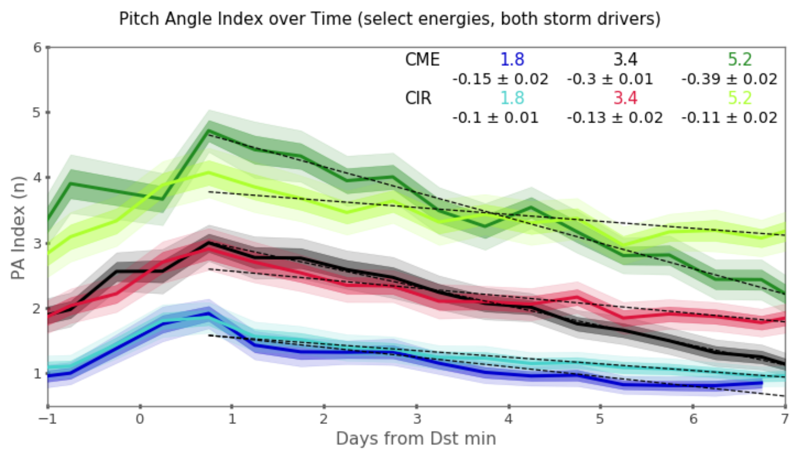

Figure 7. Superposed epoch study of PAD evolution for for electrons of energies 1.8, 3.4, and 5.2 MeV, for CME- and CIR-driven storms. CME(CIR) curves are shown in dark(light) colors. The CIR-driven storms are shown in light blue, red, and light green, and CME-driven storms are shown in dark blue, black, and dark green. The superposed epoch curve is shown as a solid line with shaded bands showing the 1 sigma error.

and -0.39±0.02 day^{-1} at 5.2 MeV. For CIR-driven storms, the relaxation rates are -0.10±0.01 day^{-1} for 1.8 MeV, -0.13±0.02 day^{-1} for 3.4 MeV, and -0.11±0.02 day^{-1} for 5.2 MeV in pitch angle index units per day.

From Figure 7, it is evident that the anisotropy in pitch angle distribution occurs within a day for both CME- and CIR-driven storms, but that the scale on which they occur is not the same. CIR-driven storms tend to exhibit slightly lower pitch angle anisotropies. This is true for the relativistic (1.8 MeV) and ultra relativistic (3.4 and 5.2 MeV) electrons. A clear energy dependence is seen in the rate at which PADs isotropize for CME-driven storms, and the isotoprization rate more than doubles between the 1.8 and 5.2 MeV energy bins. The isotropization rates for CIR-driven storms changes between energy channels, but there is not a clear energy dependence. The isotropization rate for CME-driven storms is higher than the CIR-driven storms in each energy channel, but it diverges the most at higher energies. The slopes are statistically different for each energy channel.

5 Discussion

The individual storm analysis results show that relativistic and ultra relativistic electrons are associated with strong anisotropies soon after storm main phase. In addition, we found that between any two energy channels, the higher energy electrons are more anisotropic than the lower energy electrons during every storm with enhancements analyzed. Relativistic and ultra relativistic electrons are either energized around 90° or energize isotropically and quickly anisotropize after energization due to strong pitch angle diffusion into the loss cone. We cannot differentiate between the two when instrument measurements are many hours apart.

Previous studies have found that wave-particle interactions are most effective at accelerating relativistic energy electrons (Thorne, 2010). More recently, studies have shown that a combination of wave-particle interactions and radial diffusion can be an effective acceleration combination during geomagnetic storms (Zhao, Baker, Li, Malaspina, et al., 2019; Jaynes et al., 2018). Jaynes et al. (2018) found that ULF wave acceleration followed by inward radial diffusion can energize source populations to ultra relatitivstic energies. Electrons with pitch angles near 90° are more effectively energized by radial diffusion (Chen et al., 2007; Lejosne & Kollmann, 2020), which may explain the anisotropies of the higher energy electrons, and why pitch angles appear to become more anisotropic on similar timescales. This is consistent with our results, which show the most anisotropy at the highest energies in the day after Dst minimum.

From our results, it is evident that pitch angle distributions also isotropize on similar time scales across a wide range of energies. Wave-particle interactions via cyclotron resonance may not be able to interact with electrons from relativistic all the way to ultra relativistic energies. For example, the effect of EMIC waves on precipitation via cyclotron resonance is well studied (Jordanova et al., 2001; Summers & Thorne, 2003). The EMIC wave minimum resonance energy for cyclotron resonance is most often above $\sim$2 MeV (Meredith et al., 2003; Summers & Thorne, 2003) but most effectively scatters lower pitch angles into the loss cone, so would be unable to account for isotropization, much less in all observed REPT energy channels. However, if other types of resonances are considered, such as Landau or bounce, the energy range affected broadens dramatically and may in fact play a dominant role in the isotropization rates of energetic electrons.

More recent results from Fu et al. (2018) show that quasilinear Landau resonance interactions are less likely to cause precipitation, but can pitch angle scatter near equatorial electrons to lower pitch angles. This is especially striking due to its effectiveness across a wide range of energies, from 10s of keV to 10 MeV. Another recent study shows that nonlinear Landau trapping can effectively pitch angle scatter energetic electrons from 89° to 80° in a matter of seconds (Wang et al., 2016). They showed effective scattering results from 10 keV to 5 MeV, but did not test the upper energy limit, so this scattering may continue to even higher energies. We suggest, therefore, at multi MeV energies, Landau resonance could play an important role in EMIC wave pitch angle scattering near 90° even while the cyclotron resonance is unable to scatter lower pitch angles into the loss cone.

Chorus waves and hiss have also been shown to have non cyclotron resonant interactions that can affect a wide range of energetic electrons. Chorus waves may affect the second adiabatic invariant, and scatter relativistic electrons near the equator (Shprits, 2009). Fu et al. (2020) shows that in addition, hiss can bounce and Landau resonate with equatorial pitch angles. They claim that hiss may be an important mechanism in the evolution of pitch angle distributions. Ultimately, there may be a variety of waves that can interact with relativistic and ultra relativistic electrons via Landau and bounce resonances. The recent modeling (Wang et al., 2016; Fu et al., 2020; Shprits, 2009) of nonlinear and non cyclotron resonant interactions are one possible mechanism by which ultra relativistic electrons isotropize during storm recovery, but their full contribution to radiation belt dynamics still needs to be explored. Our results indicate that these types of interactions may potentially dominate during and after geomagnetic storms. The connection between effective pitch angle scattering and Landau resonance would be an interesting future topic for study.

We can also draw the following conclusions from the superposed epoch analysis of pitch angle index changes. For all storm drivers, pitch angle distributions are most anisotropic within one day after Dst minimum. Subsequently, the pitch angle distributions isotropize over time, but at different rates, depending on the storm driver. This result agrees with and furthers the work of other studies, which qualitatively state that pitch angle distributions isotropize after storms (Lyons & Williams, 1975; Ni et al., 2015). This isotropization could mean that either electrons diffuse in pitch angle faster during CME-driven storms, or there are continual injections at large pitch angles during CIR-driven storms that affect the overall distribution shape.

As mentioned in Section 4.1, the electron dropouts that are observed during the main phase of geomagnetic storms can be due to a combination of adiabatic and nonadiabatic changes. With adiabatic changes, the electrons seem to disappear during main phase and reappear during recovery, from the point of view of a sensor with a fixed energy threshold of detection. When the ring current is enhanced, the Dst index drops, and the magnetic flux enclosed by the particle drift shell decreases. In order to conserve the third adiabatic invariant, the drift shell expands in L. Then, the magnetic field is smaller, and to conserve the first adiabatic invariant, kinetic energy decreases (J. Roederer, 1970). A larger storm (Dst<-100 nT) may have a drift shell change of up to 1 in L, while a storm around Dst=-50nT may drift outwards by $\sim$0.5 R_E (Kim & Chan, 1997). As the Dst index recovers, these electrons drift inwards and regain energy, which could account for some of the poststorm flux in some storms. However, the larger storms in this study (Dst $<$ -100 nT) tended to have a poststorm maxima that were at a smaller R_E than the prestorm flux, indicating nonadiabatic changes. In addition, the fact that the electron intensities were high even in the higher energy channels indicates that these electrons are newly energized (see Section 4.1). In this study, we focus on the poststorm electron population in order to examine the nature of PAD evolution of energized electrons. Our study extends earlier studies (Kanekal et al., 2005, 2001; G. Reeves et al., 1998) to explore the connection between pitch angle scattering and energization by using energetic electron data, which covers a wider range of pitch angles, energies, and from a near equatorial plane.

Two potential limitations of our study are due to butterfly pitch angle distributions and pitch angle distribution differences due to the Van Allen Probes orbit traversing a range of magnetic latitude. Butterfly distributions are poorly fit with a $sin^n\theta$ function, and are not easily labeled as 'anisotropic' or 'isotropic.' However, we found that, overall, the number of butterfly PADs was relatively small. In the five days after Dst minimum, butterfly PADs made up <2% of the total number of fits in the 1.8-4.2 MeV electron energy channels . They accounted for $\sim$4% of the fits in the 5.2 MeV channel, but at 6.3 MeV they made up almost 25% of the fits. The analysis in this study focuses on the 1.8-5.2 MeV electrons, thus the butterfly PADs do not significantly affect our results.

The magnetic latitude of the spacecraft can affect PAD, making them appear more anisotropic off the equator than equatorial measurements would show. Zhao et al. (2014) found that pitch angle distributions as little as 10 degrees off the equator could affect the distribution measurement. However, in our superposed epoch analysis, restricting |MLAT| to $< 5°$ did not alter the isotropization rates greater than the fit error. In addition, the results from the single storm analyses are qualitative and would not be affected by small changes in the pitch angle index. Even if some of the pitch angle distributions were slightly lower at the equator, the behavior analyzed (i.e. higher energies associated with higher anisotropy) is unaffected by this shift.

6 Summary

In this study, we analyzed evolution of pitch angle distributions of relativistic and ultra relativistic electrons in geomagnetic storms with enhancements in the ultra relativistic energy range. The study investigated the temporal evolution of pitch angle indices obtained from fitting PADs of electrons spanning energy ranges from 1.8 to 7.7 MeV for individual storms with the functional form $J_0 sin^n\theta$. The results of this study indicated that within storms, electron pitch angle distributions vary nearly simultaneously across energy channels, from relativistic to ultra relativistic energies. That is, an increase in the pitch angle index at relativistic energies was reflected in the ultra relativistic energies, both both decreased in pitch angle indices at the same time, although ultra relativistic electrons always had more anisotropic PADs than relativistic electrons.

We then performed a superposed epoch analysis of electron pitch angle index and compared electrons of the same energy across different storms. We found that electrons exhibit pitch angle coherence over a wide range of energies, and that pitch angle distributions change in the same manner across energies. Pitch angles consistently became more anisotropic in the day following Dst minimum of each storm. They then became more isotropic in the following week, at rates that were different for CME- and CIR- driven storms. The results of this study indicate a remarkable coherence, and emphasizes that there is more work to be done in regards to understanding the energization of electrons in the outer radiation belt.

We also investigated the temporal evolution of electron PADs for solar driver dependence, i.e., CME- and CIR- driven geomagnetic storms. Storms driven by CMEs have more anisotropic pitch angle distributions in the day following Dst minimum, and more rapidly isotropize to prestorm values after a storm than do CIR-driven storms. However the overall temporal behavior is the same between the storm drivers. This is true across relativistic and ultra relativistic electrons, suggesting that both energy regimes are accelerated in the same manner.

In summary, we found that pitch angle distributions are energy dependent, and that consecutively higher energies are consistently more anisotropic after storm onset. We also found that pitch angle indices generally peak within a day of Dst_{min} and isotropization back to prestorm values can be fit linearly. CME-driven storms are both more anisotropic and have faster rates of isotropization than do CIR-driven storms. These may be caused by wave-particle interactions or a combination of wave-particle interactions and inward radial diffusion, prominent during storm times.

Acknowledgments

A list of storms used can be found in supporting information. Van Allen Probes data are publicly accessible at https://rbspgway.jhuapl.edu and https://rbsp-ect.lanl.gov/rbsp_ect.php. This research was supported by an appointment to the NASA Postdoctoral Program at the NASA Goddard Space Flight Center, administered by Universities Space Research Association under contract with NASA. Research was also supported by the International Space Science Institute's (ISSI) International Teams program.

References

Baker, D. N., Higbie, P. R., Hones Jr., E. W., & Belian, R. D. (1978). High-resolution energetic particle measurements at 6.6 re 3. low-energy electron anisotropies and short-term substorm predictions. *Journal of Geophysical Research: Space Physics*, *83*(A10), 4863-4868. Retrieved from `https://agupubs.onlinelibrary.wiley.com/doi/abs/10.1029/JA083iA10p04863` doi: 10.1029/JA083iA10p04863

Baker, D. N., Jaynes, A. N., Li, X., Henderson, M. G., Kanekal, S. G., Reeves, G. D., . . . Shprits, Y. Y. (2014). Gradual diffusion and punctuated phase space density enhancements of highly relativistic electrons: Van allen probes observations. *Geophysical Research Letters*, *41*(5), 1351-1358. Retrieved from `https://agupubs.onlinelibrary.wiley.com/doi/abs/10.1002/2013GL058942` doi: 10.1002/2013GL058942

Baker, D. N., Kanekal, S. G., Hoxie, V. C., Henderson, M. G., Li, X., Spence, H. E., . . . Claudepierre, S. G. (2013). A long-lived relativistic electron storage ring embedded in earth's outer van allen belt. *Science*, *340*(6129), 186–190. Retrieved from `https://science.sciencemag.org/content/340/6129/186` doi: 10.1126/science.1233518

Baker, D. N., et al. (2012). The relativistic electron-proton telescope (rept) instrument on board the radiation belt storm probes (rbsp) spacecraft: Characterization of earth's radiation belt high-energy particle populations. *Space Sci. Rev.*, *179*, 1-4. doi: 10.1007/s11214-012-9950-9

Bingham, S. T., Mouikis, C. G., Kistler, L. M., Boyd, A. J., Paulson, K., Farrugia, C. J., ... Kletzing, C. (2018). The outer radiation belt response to the storm time development of seed electrons and chorus wave activity during cme and cir driven storms. *Journal of Geophysical Research: Space Physics*, *123*(12), 10,139-10,157. Retrieved from https://agupubs.onlinelibrary.wiley.com/doi/abs/10.1029/2018JA025963 doi: 10.1029/2018JA025963

Blake, J. B., Selesnick, R. S., Baker, D. N., & Kanekal, S. (2001). Studies of relativistic electron injection events in 1997 and 1998. *Journal of Geophysical Research: Space Physics*, *106*(A9), 19157-19168. Retrieved from https://agupubs.onlinelibrary.wiley.com/doi/abs/10.1029/2000JA003039 doi: 10.1029/2000JA003039

Carbary, J. F., Mitchell, D. G., Paranicas, C., Roelof, E. C., Krimigis, S. M., Krupp, N., ... Dougherty, M. (2011). Pitch angle distributions of energetic electrons at saturn. *Journal of Geophysical Research: Space Physics*, *116*(A1). Retrieved from https://agupubs.onlinelibrary.wiley.com/doi/abs/10.1029/2010JA015987 doi: 10.1029/2010JA015987

Chen, Y., Friedel, R. H. W., Henderson, M. G., Claudepierre, S. G., Morley, S. K., & Spence, H. E. (2014). Repad: An empirical model of pitch angle distributions for energetic electrons in the earth's outer radiation belt. *Journal of Geophysical Research: Space Physics*, *119*(3), 1693-1708. Retrieved from https://agupubs.onlinelibrary.wiley.com/doi/abs/10.1002/2013JA019431 doi: 10.1002/2013JA019431

Chen, Y., Reeves, G. D., & Friedel, R. H. W. (2007). The energization of relativistic electrons in the outer van allen radiation belt. *Nature Physics*, *3*(9), 614–617. Retrieved from https://doi.org/10.1038/nphys655 doi: 10.1038/nphys655

Claudepierre, S. G., Elkington, S. R., & Wiltberger, M. (2008). Solar wind driving of magnetospheric ulf waves: Pulsations driven by velocity shear at the magnetopause. *Journal of Geophysical Research: Space Physics*, *113*(A5). Retrieved from https://agupubs.onlinelibrary.wiley.com/doi/abs/10.1029/2007JA012890 doi: 10.1029/2007JA012890

Fennell, J. F., Roeder, J. L., Kurth, W. S., Henderson, M. G., Larsen, B. A., Hospodarsky, G., ... Reeves, G. D. (2014). Van allen probes observations of direct wave-particle interactions. *Geophysical Research Letters*, *41*(6), 1869-1875. Retrieved from https://agupubs.onlinelibrary.wiley.com/doi/abs/10.1002/2013GL059165 doi: 10.1002/2013GL059165

Finlay, C. C., Maus, S., Beggan, C. D., Bondar, T. N., Chambodut, A., Chernova, T. A., ... Zvereva, T. I. (2010, 12). International Geomagnetic Reference Field: the eleventh generation. *Geophysical Journal International*, *183*(3), 1216-1230. Retrieved from https://doi.org/10.1111/j.1365-246X.2010.04804.x doi: 10.1111/j.1365-246X.2010.04804.x

Fu, S., Ni, B., Lou, Y., Bortnik, J., Ge, Y., Tao, X., ... Wang, Q. (2018). Resonant scattering of near-equatorially mirroring electrons by landau resonance with h+ band emic waves. *Geophysical Research Letters*, *45*(20), 10,866-10,873. Retrieved from https://agupubs.onlinelibrary.wiley.com/doi/abs/10.1029/2018GL079718 doi: 10.1029/2018GL079718

Fu, S., Yi, J., Ni, B., Zhou, R., Hu, Z., Cao, X., ... Guo, D. (2020). Combined scattering of radiation belt electrons by low-frequency hiss: Cyclotron, landau, and bounce resonances. *Geophysical Research Letters*, *47*(5), e2020GL086963. Retrieved from https://agupubs.onlinelibrary.wiley.com/doi/abs/10.1029/2020GL086963 (e2020GL086963 2020GL086963) doi: 10.1029/2020GL086963

Gannon, J. L., et al. (2007). Pitch angle distribution analysis of radiation belt electrons based on combined release and radiation effects satellite medium electrons a data. *J. Geophys. Res: Space Physics*, *112*(A5). Retrieved from https://agupubs.onlinelibrary.wiley.com/doi/abs/10.1029/2005JA011565 doi: 10.1029/2005JA011565

Horne, R. B., et al. (2003). Evolution of energetic electron pitch angle distributions during storm time electron acceleration to megaelectronvolt energies. *J. Geophys. Res: Space Physics*, *108*(A1), SMP 11-1-SMP 11-13. Retrieved from https://agupubs.onlinelibrary.wiley.com/doi/abs/10.1029/2001JA009165 doi: 10.1029/2001JA009165

Hudson, M. K., Baker, D. N., Goldstein, J., Kress, B. T., Paral, J., Toffoletto, F. R., & Wiltberger, M. (2014). Simulated magnetopause losses and van allen probe flux dropouts. *Geophysical Research Letters*, *41*(4), 1113-1118. Retrieved from https://agupubs.onlinelibrary.wiley.com/doi/abs/10.1002/2014GL059222 doi: 10.1002/2014GL059222

Hudson, M. K., Paral, J., Kress, B. T., Wiltberger, M., Baker, D. N., Foster, J. C., … Wygant, J. R. (2015). Modeling cme-shock-driven storms in 2012-2013: Mhd test particle simulations. *Journal of Geophysical Research: Space Physics*, *120*(2), 1168-1181. Retrieved from https://agupubs.onlinelibrary.wiley.com/doi/abs/10.1002/2014JA020833 doi: 10.1002/2014JA020833

Jaynes, A. N., Ali, A. F., Elkington, S. R., Malaspina, D. M., Baker, D. N., Li, X., … Wygant, J. R. (2018). Fast diffusion of ultrarelativistic electrons in the outer radiation belt: 17 march 2015 storm event. *Geophysical Research Letters*, *45*(20), 10,874-10,882. Retrieved from https://agupubs.onlinelibrary.wiley.com/doi/abs/10.1029/2018GL079786 doi: 10.1029/2018GL079786

Jaynes, A. N., Baker, D. N., Singer, H. J., Rodriguez, J. V., Loto'aniu, T. M., Ali, A. F., … Reeves, G. D. (2015). Source and seed populations for relativistic electrons: Their roles in radiation belt changes. *Journal of Geophysical Research: Space Physics*, *120*(9), 7240-7254. Retrieved from https://agupubs.onlinelibrary.wiley.com/doi/abs/10.1002/2015JA021234 doi: 10.1002/2015JA021234

Jian, L. (1993). *Radial evolution of large-scale solar wind structures* (Unpublished doctoral dissertation). Univ. of Calif., Los Angeles.

Jordanova, V. K., Farrugia, C. J., Thorne, R. M., Khazanov, G. V., Reeves, G. D., & Thomsen, M. F. (2001). Modeling ring current proton precipitation by electromagnetic ion cyclotron waves during the may 14-16, 1997, storm. *Journal of Geophysical Research: Space Physics*, *106*(A1), 7-22. Retrieved from https://agupubs.onlinelibrary.wiley.com/doi/abs/10.1029/2000JA002008 doi: 10.1029/2000JA002008

Kanekal, S. G. (2006). A review of recent observations of relativistic electron energization in the Earth's outer Van Allen radiation belt. In N. Gopalswamy & A. Bhattacharyya (Eds.), *Proceedings of the ilws workshop* (p. 274).

Kanekal, S. G., Baker, D. N., & Blake, J. B. (2001). Multisatellite measurements of relativistic electrons: Global coherence. *Journal of Geophysical Research: Space Physics*, *106*(A12), 29721-29732. Retrieved from https://agupubs.onlinelibrary.wiley.com/doi/abs/10.1029/2001JA000070 doi: 10.1029/2001JA000070

Kanekal, S. G., Baker, D. N., Blake, J. B., Klecker, B., Mewaldt, R. A., & Mason, G. M. (1999, November). Magnetospheric response to magnetic cloud (coronal mass ejection) events: Relativistic electron observations from SAMPEX and Polar. *Journal of Geophysics Research*, *104*, 24885-24894. doi: 10.1029/1999JA900239

Kanekal, S. G., Friedel, R. H. W., Reeves, G. D., Baker, D. N., & Blake, J. B. (2005). Relativistic electron events in 2002: Studies of pitch angle isotropization. *Journal of Geophysical Research: Space Physics*, *110*(A12). Retrieved from https://agupubs.onlinelibrary.wiley.com/doi/abs/10.1029/2004JA010974 doi: 10.1029/2004JA010974

Kasahara, S., Miyoshi, Y., Yokota, S., Mitani, T., Kasahara, Y., Matsuda, S., ... Shinohara, I. (2018). Pulsating aurora from electron scattering by chorus waves. *Nature*, *554*(7692), 337–340. Retrieved from https://doi.org/10.1038/nature25505 doi: 10.1038/nature25505

Kim, H.-J., & Chan, A. A. (1997). Fully adiabatic changes in storm time relativistic electron fluxes. *Journal of Geophysical Research: Space Physics*, *102*(A10), 22107–22116. Retrieved from https://agupubs.onlinelibrary.wiley.com/doi/abs/10.1029/97JA01814 doi: 10.1029/97JA01814

Lejosne, S., & Kollmann, P. (2020). Radiation belt radial diffusion at earth and beyond. *Space Science Reviews*, *216*(1), 19. Retrieved from https://doi.org/10.1007/s11214-020-0642-6 doi: 10.1007/s11214-020-0642-6

Li, X., Baker, D. N., Temerin, M., Cayton, T. E., Reeves, E. G. D., Christensen, R. A., ... Kanekal, S. G. (1997). Multisatellite observations of the outer zone electron variation during the november 3-4, 1993, magnetic storm. *Journal of Geophysical Research: Space Physics*, *102*(A7), 14123-14140. Retrieved from https://agupubs.onlinelibrary.wiley.com/doi/abs/10.1029/97JA01101 doi: 10.1029/97JA01101

Lyons, L. R., & Williams, D. J. (1975). The storm and poststorm evolution of energetic (35-560 kev) radiation belt electron distributions. *J. Geophys. Res*, *80*(28), 3985-3994. Retrieved from https://agupubs.onlinelibrary.wiley.com/doi/abs/10.1029/JA080i028p03985 doi: 10.1029/JA080i028p03985

Mauk, B. H., Fox, N. J., Kanekal, S. G., Kessel, R. L., Sibeck, D. G., & Ukhorskiy, A. (2013, Nov 01). Science objectives and rationale for the radiation belt storm probes mission. *Space Science Reviews*, *179*(1), 3–27. Retrieved from https://doi.org/10.1007/s11214-012-9908-y doi: 10.1007/s11214-012-9908-y

McIlwain, C. (1961). Coordinates for mapping distribution of magnetically trapped particles. *Journal of Geophysical Research*, *66*(11), 3681-&. doi: {10.1029/JZ066i011p03681}

Meredith, N. P., Thorne, R. M., Horne, R. B., Summers, D., Fraser, B. J., & Anderson, R. R. (2003). Statistical analysis of relativistic electron energies for cyclotron resonance with emic waves observed on crres. *Journal of Geophysical Research: Space Physics*, *108*(A6). Retrieved from https://agupubs.onlinelibrary.wiley.com/doi/abs/10.1029/2002JA009700 doi: 10.1029/2002JA009700

Miyoshi, Y., Shinohara, I., Takashima, T., Asamura, K., Higashio, N., Mitani, T., ... Seki, K. (2018). Geospace exploration project erg. *Earth, Planets and Space*, *70*(1), 101. Retrieved from https://doi.org/10.1186/s40623-018-0862-0 doi: 10.1186/s40623-018-0862-0

Moré, J. J. (1978). The levenberg-marquardt algorithm: Implementation and theory. In G. A. Watson (Ed.), *Numerical analysis* (pp. 105–116). Berlin, Heidelberg: Springer Berlin Heidelberg.

Mourenas, D., Artemyev, A. V., Agapitov, O. V., & Krasnoselskikh, V. (2014). Consequences of geomagnetic activity on energization and loss of radiation belt electrons by oblique chorus waves. *Journal of Geophysical Research: Space Physics*, *119*(4), 2775-2796. Retrieved from https://agupubs.onlinelibrary.wiley.com/doi/abs/10.1002/2013JA019674 doi: 10.1002/2013JA019674

Neugebauer, M., & Goldstein, R. (2013). Particle and field signatures of coronal mass ejections in the solar wind. In *Coronal mass ejections* (p. 245-251). American Geophysical Union (AGU). Retrieved from https://agupubs.onlinelibrary.wiley.com/doi/abs/10.1029/GM099p0245 doi: 10.1029/GM099p0245

Ni, B., et al. (2015). Variability of the pitch angle distribution of radiation belt ultrarelativistic electrons during and following intense geomagnetic storms: Van allen probes observations. *J. Geophys. Res: Space Physics*, *120*(6), 4863-4876. Retrieved from https://agupubs.onlinelibrary.wiley.com/doi/abs/10.1002/2015JA021065 doi: 10.1002/2015JA021065

O'Brien, T. P., Lorentzen, K. R., Mann, I. R., Meredith, N. P., Blake, J. B., Fennell, J. F., ... Anderson, R. R. (2003). Energization of relativistic electrons in the presence of ulf power and mev microbursts: Evidence for dual ulf and vlf acceleration. *Journal of Geophysical Research: Space Physics*, *108*(A8). Retrieved from https://agupubs.onlinelibrary.wiley.com/doi/abs/10.1029/2002JA009784 doi: 10.1029/2002JA009784

Olson, W., & Pfitzer, K. (1977). Magnetospheric magnetic field modeling. *Tech. Rep., McDonnell Douglas Astronaut. Co., Huntington Beach, Calif.*.

Reeves, G., Cayton, T., Friedel, R., Jahn, J., Henderson, M., Meier, M., ... others (1998). Relativistic electron observations in the three-dimensional magnetosphere. *Eos Trans, AGU*, *79*, 17.

Reeves, G. D., McAdams, K. L., Friedel, R. H. W., & O'Brien, T. P. (2003). Acceleration and loss of relativistic electrons during geomagnetic storms. *Geophysical Research Letters*, *30*(10). Retrieved from https://agupubs.onlinelibrary.wiley.com/doi/abs/10.1029/2002GL016513 doi: 10.1029/2002GL016513

Reeves, G. D., Spence, H. E., Henderson, M. G., Morley, S. K., Friedel, R. H. W., Funsten, H. O., ... Niehof, J. T. (2013). Electron acceleration in the heart of the van allen radiation belts. *Science*, *341*(6149), 991–994. Retrieved from https://science.sciencemag.org/content/341/6149/991 doi: 10.1126/science.1237743

Richardson, I., & Cane, H. (2019). *Near-earth interplanetary coronal mass ejections since january 1996.* Retrieved 2019-08-28, from http://www.srl.caltech.edu/ACE/ASC/DATA/level3/icmetable2.htm

Roederer, J. (1970). Dynamics of geomagnetically trapped radiation. In *Physics and chemistry in space* (Vol. Vol. 2). Berlin: Springer.

Roederer, J. G. (1967). On the adiabatic motion of energetic particles in a model magnetosphere. *Journal of Geophysical Research*, *72*(3), 981–992. Retrieved from http://dx.doi.org/10.1029/JZ072i003p00981 doi: 10.1029/JZ072i003p00981

Selesnick, R. S., & Blake, J. B. (2002). Relativistic electron drift shell splitting. *J. Geophys. Res: Space Physics*, *107*(A9), SMP 27-1-SMP 27-10. Retrieved from https://agupubs.onlinelibrary.wiley.com/doi/abs/10.1029/2001JA009179 doi: 10.1029/2001JA009179

Shen, X., Hudson, M. K., Jaynes, A. N., Shi, Q., Tian, A., Claudepierre, S. G., ... Sun, W. (2017, 8). Statistical study of the storm time radiation belt evolution during van allen probes era: Cme- versus cir-driven storms. *Journal of Geophysical Research: Space Physics*, *122*(8), 8327–8339. Retrieved from https://doi.org/10.1002/2017JA024100 doi: 10.1002/2017JA024100

Shprits, Y. Y. (2009). Potential waves for pitch-angle scattering of near-equatorially mirroring energetic electrons due to the violation of the second adiabatic invariant. *Geophysical Research Letters*, *36*(12). Retrieved from https://agupubs.onlinelibrary.wiley.com/doi/abs/10.1029/2009GL038322 doi: 10.1029/2009GL038322

Sibeck, D., Kanekal, S., Fox, N., Mauk, B., & Kessel, R. (2012, 07). The radiation belt storm probes mission: Advancing our understanding of the earth's radiation belts. , 1806-.

Sibeck, D. G., et al. (1987). Magnetic field drift shell splitting: Cause of unusual dayside particle pitch angle distributions during storms and substorms. *J. Geophys. Res: Space Physics*, *92*(A12), 13485-13497. Retrieved from https://

agupubs.onlinelibrary.wiley.com/doi/abs/10.1029/JA092iA12p13485 doi: 10.1029/JA092iA12p13485

Stone, E. C. (1963). The physical significance and application of l, b_0, and r_0 to geomagnetically trapped particles. *J. Geophys. Res*, *68*(14), 4157-4166.

Summers, D., & Thorne, R. M. (2003). Relativistic electron pitch-angle scattering by electromagnetic ion cyclotron waves during geomagnetic storms. *Journal of Geophysical Research: Space Physics*, *108*(A4). Retrieved from https://agupubs.onlinelibrary.wiley.com/doi/abs/10.1029/2002JA009489 doi: 10.1029/2002JA009489

Summers, D., Thorne, R. M., & Xiao, F. (1998). Relativistic theory of wave-particle resonant diffusion with application to electron acceleration in the magnetosphere. *Journal of Geophysical Research: Space Physics*, *103*(A9), 20487-20500. Retrieved from https://agupubs.onlinelibrary.wiley.com/doi/abs/10.1029/98JA01740 doi: 10.1029/98JA01740

Thorne, R. M. (2010). Radiation belt dynamics: The importance of wave-particle interactions. *Geophysical Research Letters*, *37*(22). Retrieved from https://agupubs.onlinelibrary.wiley.com/doi/abs/10.1029/2010GL044990 doi: 10.1029/2010GL044990

Thorne, R. M., Li, W., Ni, B., Ma, Q., Bortnik, J., Baker, D. N., … Angelopoulos, V. (2013). Evolution and slow decay of an unusual narrow ring of relativistic electrons near l? ?3.2 following the september 2012 magnetic storm. *Geophysical Research Letters*, *40*(14), 3507-3511. Retrieved from https://agupubs.onlinelibrary.wiley.com/doi/abs/10.1002/grl.50627 doi: 10.1002/grl.50627

Thorne, R. M., Li, W., Ni, B., Ma, Q., Bortnik, J., Chen, L., … Kanekal, S. G. (2013). Rapid local acceleration of relativistic radiation-belt electrons by magnetospheric chorus. *Nature*, *504*(7480), 411–414. Retrieved from https://doi.org/10.1038/nature12889 doi: 10.1038/nature12889

Turner, D. L., Morley, S. K., Miyoshi, Y., Ni, B., & Huang, C.-L. (2013). Outer radiation belt flux dropouts: Current understanding and unresolved questions. In *Dynamics of the earth's radiation belts and inner magnetosphere* (p. 195-212). American Geophysical Union (AGU). Retrieved from https://agupubs.onlinelibrary.wiley.com/doi/abs/10.1029/2012GM001310 doi: 10.1029/2012GM001310

Turner, D. L., O'Brien, T. P., Fennell, J. F., Claudepierre, S. G., Blake, J. B., Kilpua, E. K. J., & Hietala, H. (2015). The effects of geomagnetic storms on electrons in earth's radiation belts. *Geophysical Research Letters*, *42*(21), 9176-9184. Retrieved from https://agupubs.onlinelibrary.wiley.com/doi/abs/10.1002/2015GL064747 doi: 10.1002/2015GL064747

Wang, B., Su, Z., Zhang, Y., Shi, S., & Wang, G. (2016). Nonlinear landau resonant scattering of near equatorially mirroring radiation belt electrons by oblique emic waves. *Geophysical Research Letters*, *43*(8), 3628-3636. Retrieved from https://agupubs.onlinelibrary.wiley.com/doi/abs/10.1002/2016GL068467 doi: 10.1002/2016GL068467

West Jr., H. I., et al. (1973). Electron pitch angle distributions throughout the magnetosphere as observed on ogo 5. *J. Geophys. Res*, *78*(7), 1064-1081. Retrieved from https://agupubs.onlinelibrary.wiley.com/doi/abs/10.1029/JA078i007p01064 doi: 10.1029/JA078i007p01064

Zhao, H., Baker, D., Li, X., Malaspina, D., Jaynes, A., & Kanekal, S. (2019). On the acceleration mechanism of ultrarelativistic electrons in the center of the outer radiation belt: A statistical study. *Journal of Geophysical Research: Space Physics*, *124*(11), 8590-8599. Retrieved from https://agupubs.onlinelibrary.wiley.com/doi/abs/10.1029/2019JA027111 doi: 10.1029/2019JA027111

Zhao, H., Baker, D. N., Li, X., Jaynes, A. N., & Kanekal, S. G. (2019). The effects of geomagnetic storms and solar wind conditions on the ultrarelativistic electron flux enhancements. *J. Geophys. Res: Space Physics*, *124*(3), 1948-1965. Retrieved from https://agupubs.onlinelibrary.wiley.com/doi/abs/10.1029/2018JA026257 doi: 10.1029/2018JA026257

Zhao, H., Li, X., Blake, J. B., Fennell, J. F., Claudepierre, S. G., Baker, D. N., ... Kanekal, S. G. (2014). Peculiar pitch angle distribution of relativistic electrons in the inner radiation belt and slot region. *Geophysical Research Letters*, *41*(7), 2250-2257. Retrieved from https://agupubs.onlinelibrary.wiley.com/doi/abs/10.1002/2014GL059725 doi: 10.1002/2014GL059725

Zhao, H., et al. (2018). An empirical model of radiation belt electron pitch angle distributions based on van allen probes measurements. *J. Geophys. Res: Space Physics*, *123*(5), 3493-3511. Retrieved from https://agupubs.onlinelibrary.wiley.com/doi/abs/10.1029/2018JA025277 doi: 10.1029/2018JA025277